Outline

1 Ray-tracing and Fokker-Planck coupling

The coupling of the AMR (Antenna, Mode-conversion, Ray-tracing) code and the LUKE code [1] started in 2008 and the interface was successively improved during the following years. LUKE is a fully relativistic, bounce-averaged, 3-D Fokker-Planck solver, which calculates the evolution of the electron distribution function for axisymmetric plasmas in the low-collisionality regime. LUKE particularly accounts for collisions and quasilinear diffusion induced by RF waves. The code uses a fully-relativistic, parallel momentum conserving collision operator and a fully implicit 3-D time evolution scheme for fast convergence to a time-asymptotic solution. AMR is an EBW ray-tracing and mode-conversion code, specifically developed for spherical tokamaks, which we were routinely using for EBW emission experiments analysis from NSTX [2-6].

The coupling of the two codes is achieved as follows. After determining the initial wave vector from the dispersion relation, the electrostatic ray-tracing is initiated. The principal results are the evolution of the ray trajectories and wave vectors. When the ray-tracing is completed, the outputs are passed to LUKE, together with the magnetic equilibrium and plasma profiles. Optionally, the conversion efficiency can be calculated by AMR and taken into account. The AMR-LUKE interface has been particularly verified for consistency. The interface is user friendly with LUKE able to be launched by AMR (and vice versa) by a single option in the configuration file.

The principal outputs of the coupled codes are the radial profiles of the power deposition and current drive by the electron Bernstein waves. These capabilities have been successfully employed for EBW heating and current drive studies, as described hereinafter.

2 Relativistic and electromagnetic effects in EBW damping (ray-tracing)

Relevant publication: [7]

We have compared several damping models implemented in our ray-tracing code examining, in particular the effects of the relativistic damping corrections and the electrostatic approximation under realistic tokamak conditions. Except for the non-relativistic damping term, we implemented and compared the weakly relativistic damping model of Decker & Ram [8], the weakly-relativistic model due to Saveliev [9] and a routine that integrates numerically the fully-relativistic dispersion tensor in the momentum space along the resonance curve [10].

The relative computational times are compared in Figure 1. Several points can be drawn from many different parameter runs:

- Non-relativistic damping overestimates low field side (LFS) damping while it underestimates the high field side (HFS) damping. The error can be critical and thus non-relativistic damping should be avoided in EBW simulations.
- The weakly-relativistic model of Decker & Ram [8] somewhat overestimates both LFS and HFS damping. However, the error is reasonable considering the simplicity of this model. Attention must be paid to the validity limits, which are sometimes broken. The computation time is almost identical to the non-relativistic model (and can even be shorter in those cases when the ray lengths are shorter).
- The Saveliev and the fully-relativistic model yield almost identical results (a minor deviation can be seen at 22 GHz frequency). The speed of the fully-relativistic calculation is not much longer than the non- or weakly-relativistic case if p_{n0}=5 or 10, where 10 is a reasonably safe value. Saveliev formula takes much longer time to evaluate, particularly if high accuracy is required. Limitation to $\Im(D_{\mathrm{WR}}) > D_0$ does not considerably improve the performance.

If computational speed is of critical importance, the Decker & Ram weakly-relativistic damping can be used, bearing in mind its limitations. Saveliev and the fully-relativistic calculation are in good agreement. The Saveliev term seems to suffer more from numerical difficulties and also does not provide for separate harmonics damping which is necessary for current drive calculations. Hence, the fully-relativistic calculation, with a proper choice of numerical parameters, seems to be a better choice.

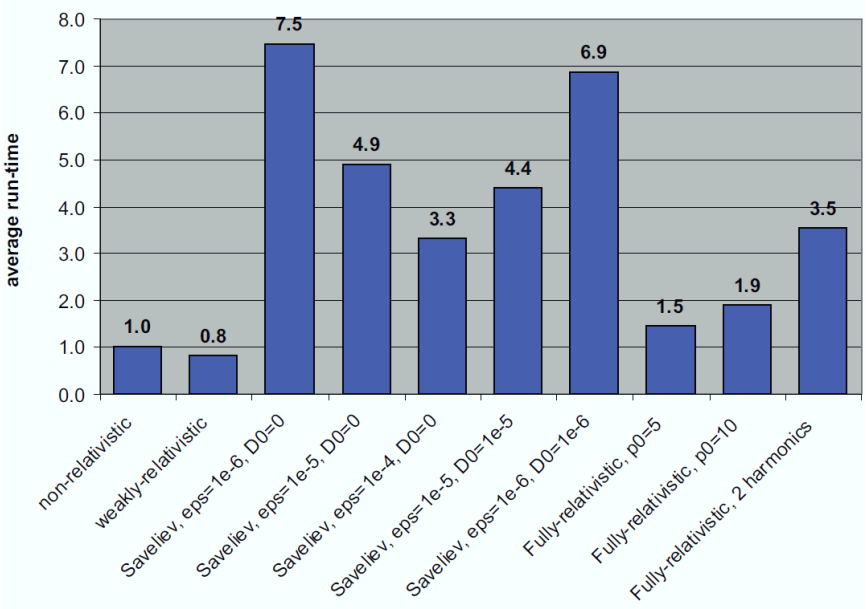

Figure 1. Average run-time for the studied damping models, normalized to the non-relativistic calculation time. eps – relative accuracy, D_0 – evaluated if $\Im(D_{\mathrm{WR}}) > D_0$, p_0 – fully-relativistic damping evaluated if the weakly-relativistic $p_n < p_0$, 2 harmonics – calculated always for n^{th} and $(n+1)^{\mathrm{th}}$ harmonics: $n\omega_{\mathrm{ce}} < \omega < (n+1)\omega_{\mathrm{ce}}$.

We have studied the differences between electrostatic (which is widely used for EBWs) and electromagnetic description of EBWs used in ray-tracing. In particularly, we have compared the wave vectors, polarizations and linear absorption coefficients. In Figure 2, we plot an example case of EBW propagation at three different frequencies in a MAST-U plasma. For this and other cases, the electrostatic approximation is best valid for the wave vector; lower accuracy appears at the damping regions. The dissipated power density can be significantly different in electrostatic and electromagnetic calculations.

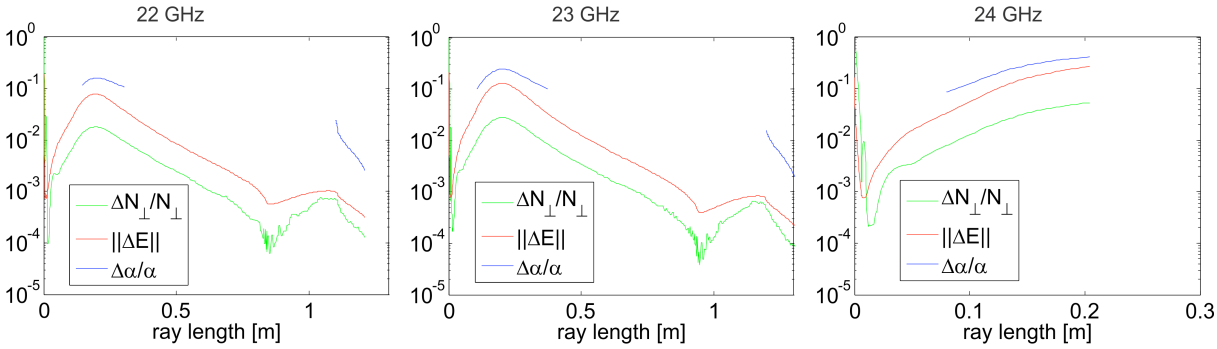

Figure 2. Relative differences between electrostatic and electromagnetic wave vectors N, polarizations E and absorbed power density α a (for a MAST-U plasma).

3 O-X-EBW mode conversion efficiency limit due to finite beam divergence

Relevant publications: [11, 12]

For the first time, a simple analytic formula for the O-X conversion efficiency of a Gaussian beam is derived from the 1D plane wave theory. Starting from the E-field of a Gaussian beam in Fourier space and using Parseval's theorem, the beam power conversion efficiency can be determined from

$$\frac{P_{\mathrm{OX}}}{P_0} = \frac{\int_{-\infty}^{\infty}\int_{-\infty}^{\infty} |E|^2 C_{\mathrm{OX}} \mathrm{d}k_x \mathrm{d}k_y}{\int_{-\infty}^{\infty}\int_{-\infty}^{\infty} |E|^2 \mathrm{d}k_x \mathrm{d}k_y}. \tag{1}$$

For the mode conversion efficiency C_{OX} we use the analytical mode conversion efficiency of a plane wave, derived by Preinhaelter [13] and Mjølhus [14], and assume a uniform magnetic field in the thin mode conversion region. Maximum conversion can be achieved when the central beam wave vector is incident at the optimum angle. Under these conditions and after some algebra, the optimum beam conversion efficiency can be shown to be given by

$$\frac{P_{\mathrm{OX}}}{P_0} = \left(1 + 3\frac{\kappa}{z_{\mathrm{R}}} + 2\frac{\kappa^2}{z_{\mathrm{R}}^2}\right)^{-\frac{1}{2}}, \quad \kappa \equiv \pi L_n \sqrt{\omega_{\mathrm{ce}} / 2\omega}. \tag{2}$$

Here, $z_{\mathrm{R}} \equiv \pi w_0^2 / \lambda_0$ is the Rayleigh range, w_0 is the beam waist radius and L_n is the electron density scale length. This is an important result which, in fact, imposes an upper limit to the conversion efficiency of a Gaussian beam. This limit depends on L_n / z_{R} for a fixed $\omega_{\mathrm{ce}} / \omega$. It also tells us how narrow (i.e. how divergent) a beam can be used for efficient OXB mode conversion. As an example, in Figure 3 and Figure 4 we plot the optimum Gaussian beam conversion efficiency for typical parameters of NSTX, MAST-U and NHTX.

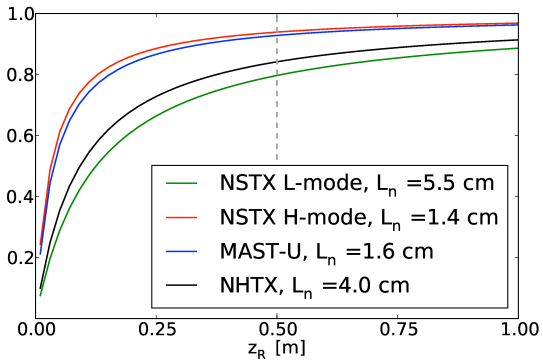

Figure 3. Gaussian beam maximum conversion efficiency (2) dependence on z_R. Average L_n in the mode conversion region is used. $\omega_{ce}/\omega = 0.5$.

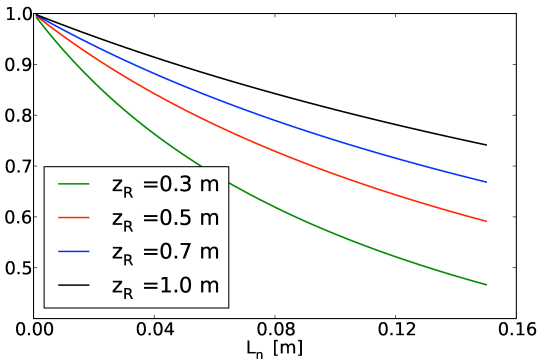

Figure 4. Gaussian beam maximum conversion efficiency (2) dependence on L_n, $\omega_{ce}/\omega = 0.5$.

4 General prospects for electron Bernstein wave heating and current drive in spherical tokamaks

Relevant publications: [11, 12, 15-22]

By means of the coupled ray-tracing and Fokker-Planck simulations, using AMR with LUKE, we have thoroughly investigated electron Bernstein wave heating and current drive prospects for spherical tokamaks, particularly for four typical present and planned plasmas: NSTX L- and H-mode, MAST Upgrade and NHTX [11, 12]. Figure 5 – Figure 8 show the current drive efficiency for the NSTX L- and H-mode, for MAST Upgrade and for NHTX. In general, from an extensive set of EBW launch scenarios with varying frequency, vertical antenna position and toroidal injection angle, it can be seen that EBW can be absorbed at almost any radius and that EBW can drive current with efficiencies comparable to that of electron cyclotron O- or X-modes. Moreover, the EBW efficiency is insensitive to the radius, while typically the X- and O-modes' efficiency decrease with radius. The best results in terms of efficiency and flexibility are achieved in the NSTX plasmas, where the electron cyclotron frequency radial profiles are monotonic. In general, normalized current drive efficiencies $|\zeta|$ on the order of 0.3 – 0.4 are feasible for all target plasmas. Absolute efficiencies depend on the actual plasma parameters with $\eta \equiv I_{RF}/P_0 \cong 0.31\zeta T_e/R_0 n_e$, where the units are A/W for η, keV for T_e, m for R_0 and $10^{19}\,\mathrm{m}^{-3}$ for n_e.

For EBWs, only the initial $N_{||}$ sign can be chosen at will, while its further evolution is determined by the wave frequency, the vertical launch position and by the plasma parameters. We have shown how different vertical launch position influences the $N_{||}$ spectrum and consequently the current drive efficiency. However, there seems to be no general correlation between the current drive efficiency and the $N_{||}$ spectrum and its width. This result is rather surprising.

Input power scans have been performed to investigate the quasilinear effects. Increasing the power generally leads to either lower or similar current drive efficiency, although contrary results exist. Higher power also causes the wave absorption to occur further in the propagation direction, which can either be towards the axis if the absorption occurs on the outboard side or away from the axis in the opposite case. An important factor is the effective ion charge, which determines the electron-ion collisionality and significantly affects the current drive efficiency. The role of Z_{eff} on the current drive location is minor as observed in the change in the plasma quasilinear response.

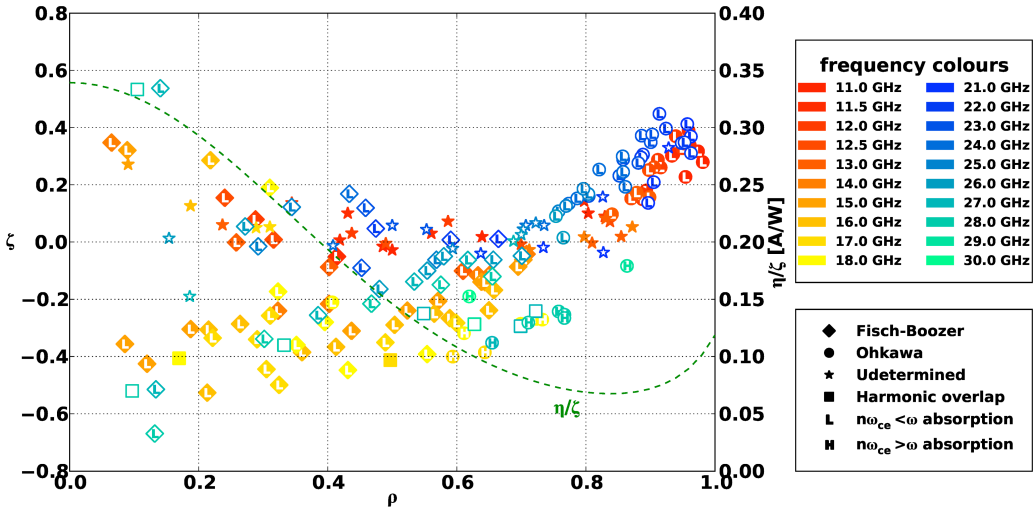

Figure 5. Current drive efficiency ζ (symbols) and η / ζ conversion factor (dashed line) versus ρ, NSTX L-mode first (full symbols) and second (open symbols) harmonics, different frequencies and launch parameters, 1 MW incident power. Neither the vertical launch position nor the $N_{\|0}$ sign can be graphically distinguished in the figure.

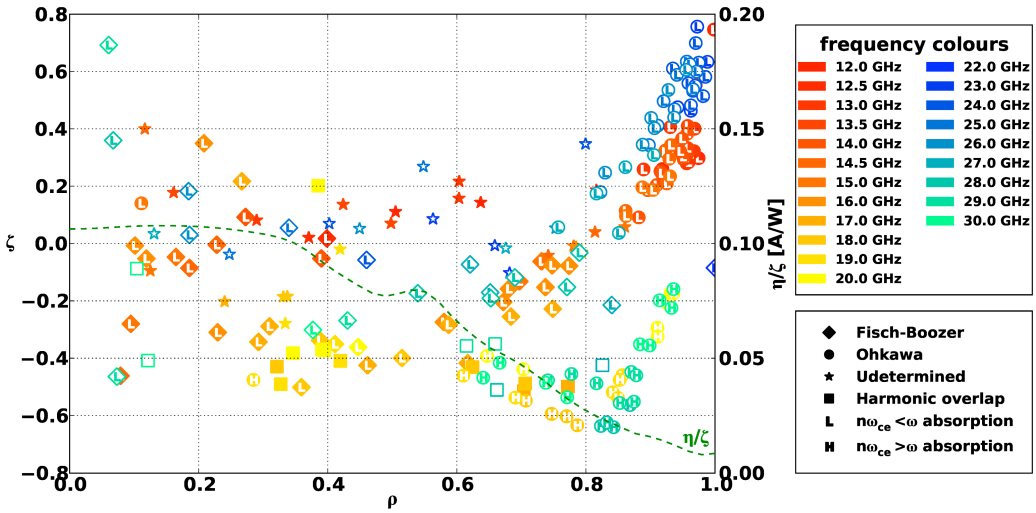

Figure 6. Same as Figure 5 but for NSTX H-mode.

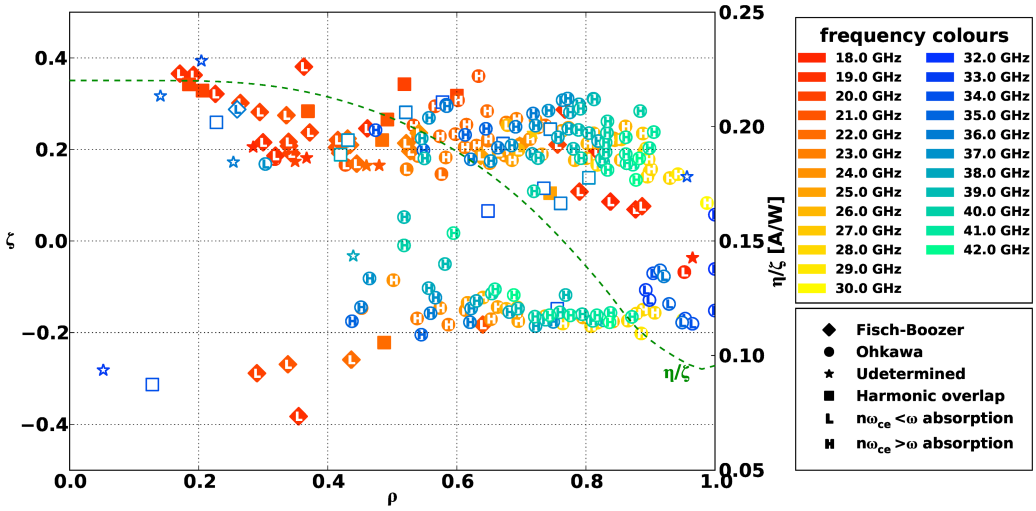

Figure 7. Same as Figure 5 but for MAST-U.

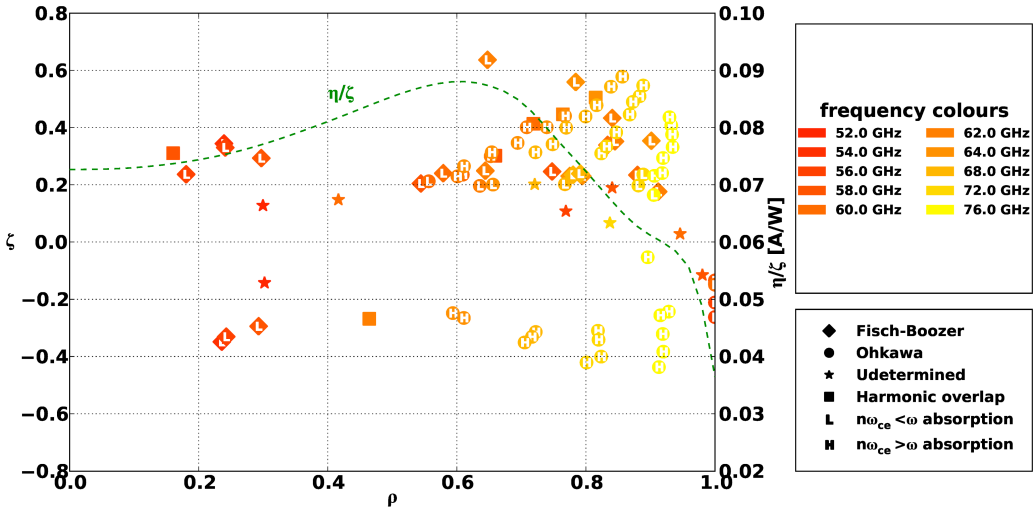

Figure 8. Same as Figure 5 but for NHTX.

5 Sensitivity of EBW H&CD

The sensitivity of EBW heating and current drive to changes in the plasma parameters has been investigated. It has been shown that the EBW performance is rather robust. Neither the current drive efficiency nor the radial location changes significantly for moderate changes in the electron temperature or density. However there is stronger sensitivity to magnetic field variations, especially in the (dominant) toroidal field.

5.1 Sensitivity to electron density and temperature profiles

In Figure 9 and Figure 10 we show the sensitivity of EBWs to plasma electron density and temperature variations in ± 50 % range. All vertical launch positions and initially both signs of $N_{\|}$ at 17 GHz NSTX L-mode cases are used to calculate the medians of the absolute location difference $\Delta\rho_{j\max}$ with the relative current drive efficiency and profile widths $|\Delta\zeta|/|\zeta_0|$ and $|\Delta\sigma_j|/|\sigma_{j0}|$, where the 0 subscripts denote results with the original plasma profiles. We first see a monotonic dependence of all the plotted quantities (except for two cases in $|\Delta\sigma_j|$), indicating a non-chaotic behavior of EBW performance with changing plasma profiles. Quantitatively, the radial current location changes fractionally compared to the typical $\sigma_j \sim 0.1$. However, very precise localization might be important for certain applications, in which case a feedback system is highly advisable. The median difference in current drive efficiency is below 5 % for less than 25 % changes in the plasma profiles, which is very favorable. The current profile width is slightly more sensitive, a consequence of Doppler broadening. Not shown here are the variances. However, highest sensitivity is generally observed at lower frequencies, close to a midplane launch where the rays tend to oscillate, leading to current drive efficiencies that are typically low. In most cases the results are close to the median values.

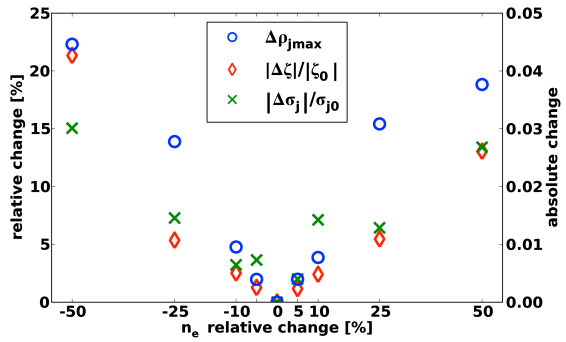

Figure 9. Medians of absolute current location difference $\Delta\rho_{j\max}$ and relative current drive efficiency and current profile width differences versus varying plasma electron density. 17 GHz NSTX L-mode 1 MW cases are used to calculate the medians.

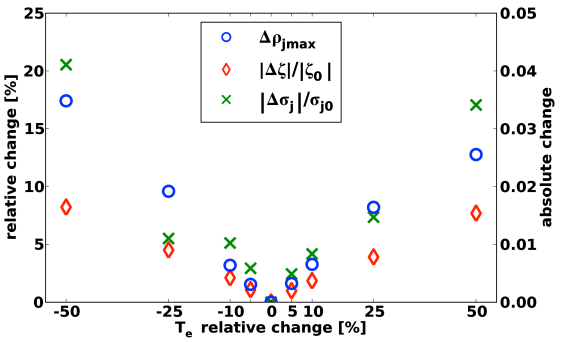

Figure 10. Same as Figure 9, but for varying electron temperature.

5.2 Sensitivity to toroidal and poloidal magnetic field

Another parameter that can vary in tokamaks is the plasma current and the toroidal magnetic field. Unlike density and temperature profiles, which are only crudely pre-programmed and evolve during the discharge, it is typical that the plasma current and toroidal magnetic field do not change during the discharge (except, of course, in the start-up and shut-down phases) and that their properties are pre-programmed with high confidence. This makes the demands on the sensitivity on these quantities less stringent as compared to the temperature and the density. In Figure 11 and Figure 12 we show the sensitivity of 17 GHz L-mode cases to poloidal and toroidal magnetic field changes. The fields are simply changed by multiplying the respective components so that the resulting equilibrium is no longer a solution of the Grad-Shafranov equation. Significantly larger effects of the magnetic field changes on EBW results can immediately be noticed. The sensitivity is particularly high for the toroidal field simply because the toroidal field is much larger than the poloidal field in most of the plasma cross-section. Also notice that changing the total magnetic field by 10 % is similar to changing the heating frequency by 1.4 GHz, which is the change in the central ω_{ce}. For large magnetic field changes we can even change the EC absorption harmonic number—e.g., decreasing B_{tor} by 25 % shifts 17 GHz into the second harmonic range.

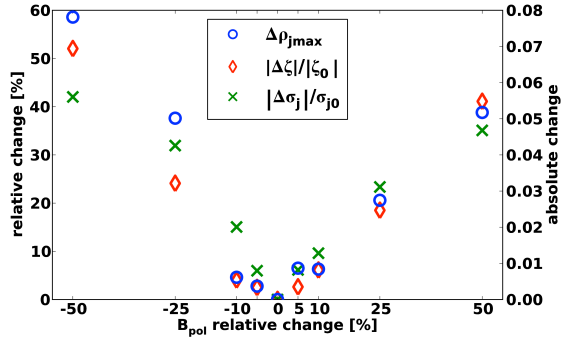

Figure 11. Same as Figure 9, but for varying poloidal magnetic field.

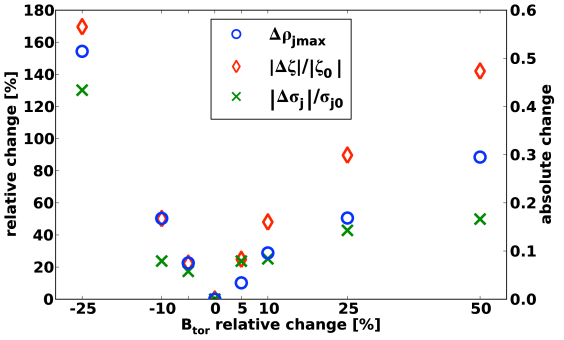

Figure 12. Same as Figure 9, but for varying toroidal magnetic field. Results for $B_{tor} - 50\%$ could not be calculated.

6 Collisional effects on EBW coupling

Relevant publications: [4-6, 15, 18, 23, 24]

Studies of collisional effects on EBW coupling were motivated by EBW emission (EBE) experiments conducted on NSTX. Extremely low level EBE signals were being detected for particular NSTX H-mode discharges. Ray-tracing and EBW-X-O conversion calculations could not initially explain this behavior. Only with the collisional damping taken into account, simulations were able to reproduce the experimental behavior. To carry out this research, the underlying theory of collisional damping effects on high frequency waves had to be revised. Successful experiments, supported by modeling using AMR, were carried out by S.J. Diem and the NSTX team [5, 6]. These experiments clarified the role of the collisional damping in EBW coupling. In particular, it was shown that EBWs can be strongly collisionally absorbed just after the mode conversion, i.e. in the upper hybrid resonance region. The main plasma parameters affecting the collisional damping are the electron temperature in the UHR region, whose position is primarily determined by the electron density profile, and the effective ion charge in that region, which is experimentally difficult to measure. In the experiments, the edge density was varied using lithium evaporation, effectively changing the UHR position and the electron temperature. Finally, a clear dependence of the EBW coupling efficiency (which takes into account the collisional damping at the UHR and the EBW-X-O mode conversion efficiency) on the electron temperature at the UHR region was shown. The effective ion charge could then be inferred from AMR simulations as it was the only unknown parameter.

In Figure 13, we show an early simulation of the temporal evolution of EBW spectrum for an NSTX H-mode shot. Clearly, without including the collisional damping (Figure 13c), the predicted EBE is very intense compared to the experimental values. Low EBE signal was not caused by low EBW-X-O conversion efficiency, as show in Figure 13b. Only the inclusion of collisional damping, as shown in Figure 13d, could, at least partially, explain the experimental observations. In Figure 14, we show a later comparison of experiment and simulation of EBE time evolution at a single frequency. $Z_{eff} = 4$ was used to obtain the best agreement.

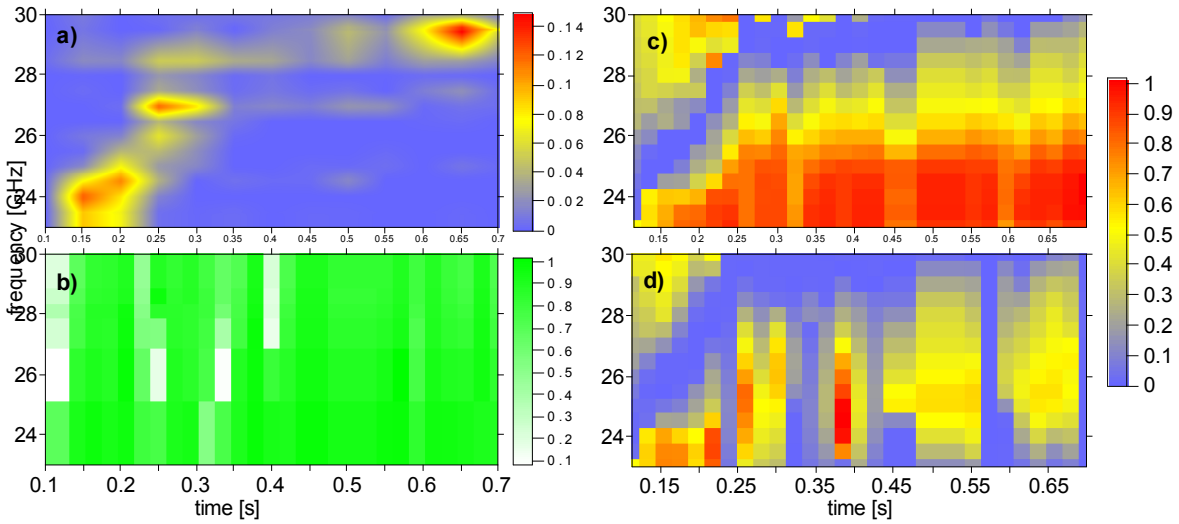

Figure 13. a) Experimental EBE T_{rad} [keV], b) simulated EBW-X-O conversion efficiency, c) simulated T_{rad} without collisions, d) simulated T_{rad} including collisions with Z_{eff}=1.5. NSTX shot 120910.

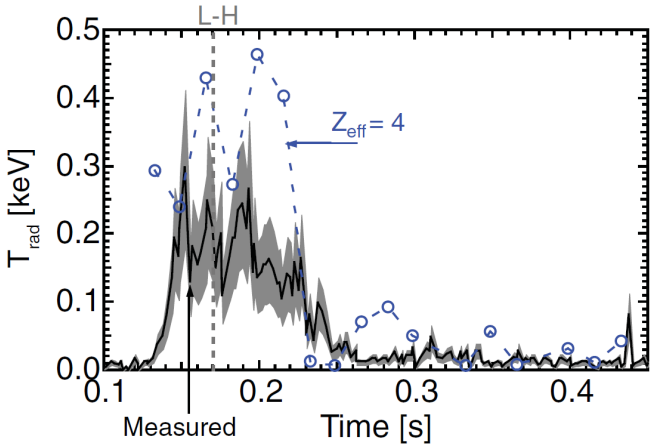

Figure 14. The measured T_{rad} (solid line) and EBE simulations of the low emission H-mode data with collisional effects, assuming $Z_{eff} = 4$ (dot-dashed line) are shown as a function of time. [6]

7 EBW propagation in a high-temperature plasma

Relevant publications: [25]

Recently, Mahajan, Kotschenreuther and Valanju (IFS, Texas) have introduced the concept of Fusion/Fission Hybrids based on the ST concept (c.f., MAST, NSTX) [26, 27]. The concept—Compact Fusion Neutron Source (CFNS)—is based on the super X divertor and the usage of fusion neutrons for rapid destruction of nuclear waste. There are many great advantages of CFNS design. Its compact, low weight fusion module within the fission blanket can be readily replaced. Fission meltdown is principally avoided.

EC or EBW current drive is foreseen to provide necessary auxiliary current drive. Other current drive methods, such as neutral beam injection, lower hybrid or ion cyclotron, are inapplicable because of their unavoidable damage caused by neutron bombardment. The efficiency of the EC/EBW current drive (like any other current drive methods) decreases with plasma collisionality. Because the electron density in the fusion neutron source is larger than 10^{20} m^{-3}, operation at high electron temperature, in the range of 20 – 35 keV, is proposed to increase the current drive efficiency to acceptable levels. However, EC waves, and particularly EBWs, can change their propagation and absorption characteristics compared to the typical electron temperatures of present day experiments. Decker and Ram [8] show that at higher temperatures, EBWs become electromagnetically polarized, as opposed to their typical quasi-electrostatic polarization at lower temperatures. Even the propagation properties can be influenced by relativistic effects, as shown by Nelson-Melby et al. [28].

We have started to study EBWs at the high temperature plasma using AMR and R2D2 [10], which is a fully relativistic dispersion solver for any EC waves (including EBWs). For CFNS parameters with central temperature of 35 keV, we performed some initial R2D2 runs; however, convergence problems seem to arise for $T_e > 15$ keV, which was rather unexpected. We also performed preliminary ray-tracing calculations, using electrostatic, non-relativistic dispersion relation for wave propagation. Figure 15 shows EBW ray trajectories in CFNS at different, scaled-down electron temperatures. Clearly, the wave propagation depends strongly on the temperature. At high temperatures, rays have difficulties to reach the central plasma due to a large Doppler shift.

Present tools, particularly AMR and R2D2, are planned to be revised and better integrated to be able to properly treat EC/EBW waves at CFNS temperature levels. The goal is to enable similar studies as presented in sections 4 and 5.

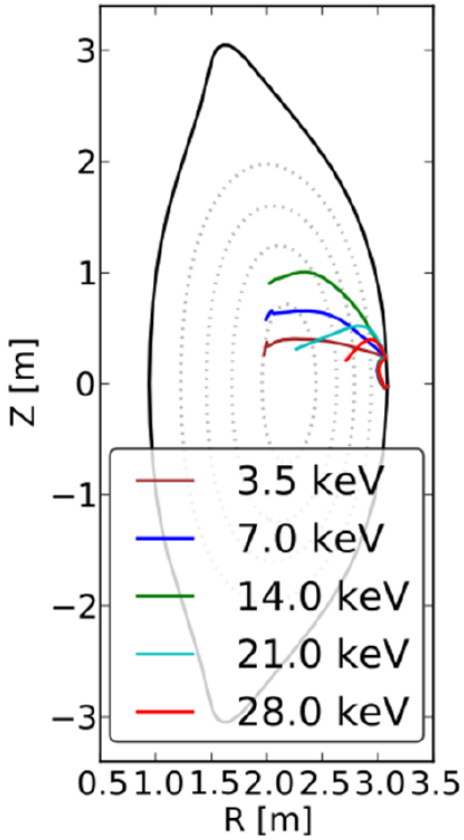

Figure 15. EBW ray trajectories in CFNS at different electron temperatures.

References

[1] J. Decker, and Y. Peysson, (EURATOM-CEA, Cadarache, 2004).
[2] J. Preinhaelter *et al.*, Rev. Sci. Inst. **77**, 10F524 (2006).
[3] J. Urban *et al.*, in *48th Annual Meeting of the Division of Plasma Physics*Philadelphia, PA, USA, 2006).
[4] J. Urban *et al.*, in 49th Annual Meeting of the Division of Plasma Physics, edited by G. Sprouse (APS, Orlando, FL, USA, 2007), pp. 304.
[5] S. J. Diem *et al.*, Phys. Rev. Lett. **103**, 015002 (2009).
[6] S. J. Diem *et al.*, Nucl. Fusion **49**, 095027 (2009).
[7] J. Urban *et al.*, in 37th EPS Conference on Plasma Physics, edited by C. McKenna (EPS, Dublin, Ireland, 2010), p. P5.191.
[8] J. Decker, and A. K. Ram, Phys. Plasmas **13**, 112503 (2006).
[9] A. N. Saveliev, Plasma Phys. Control. Fusion **49**, 1061 (2007).
[10] A. K. Ram, J. Decker, and Y. Peysson, J. Plasma Phys. **71**, 675 (2005).
[11] J. Urban *et al.*, Nucl. Fusion **51**, 083050 (2011).
[12] J. Urban *et al.*, AIP Conference Proceedings **1406**, 477 (2011).
[13] J. Preinhaelter, Czech J Phys **25**, 39 (1975).
[14] E. Mjølhus, J. Plasma Phys. **31**, 7 (1984).
[15] D. A. Gates *et al.*, Nucl. Fusion **49**, 104016 (2009).
[16] H. Meyer *et al.*, Nucl. Fusion **49**, 104017 (2009).
[17] G. Taylor *et al.*, Electron Cyclotron Emission and Electron Cyclotron Resonance Heating, 509 (2009).
[18] J. Urban *et al.*, in 51st Annual Meeting of the APS Division of Plasma Physics (American Physical Society, Atlanta, GA, USA, 2009), p. JO4.00016.

[19] J. Urban *et al.*, AIP Conference Proceedings **1187**, 465 (2009).
[20] J. Urban *et al.*, in 52nd Annual Meeting of the APS Division of Plasma Physics (American Physical Society, Chicago, IL, USA, 2010), p. BP9.00077.
[21] J. Urban *et al.*, in *16th Joint Workshop on Electron Cyclotron Emission and Electron Cyclotron Resonance Heating*Sanya, China, 2010).
[22] R. Raman *et al.*, Nucl. Fusion **51** (2011).
[23] J. Urban *et al.*, Journal of Plasma and Fusion Research SERIES **8**, 1153 (2009).
[24] S. J. Diem *et al.*, Electron Cyclotron Emission and Electron Cyclotron Resonance Heating, 226 (2009).
[25] J. Urban *et al.*, in 53rd Annual Meeting of the APS Division of Plasma Physics (American Physical Society, Salt Lake City, UT, USA, 2011), p. NP9.00077.
[26] M. Kotschenreuther *et al.*, Fusion Eng. Des. **84**, 83 (2009).
[27] M. Kotschenreuther *et al.*, Nucl. Fusion **50** (2010).
[28] E. Nelson-Melby *et al.*, Plasma Phys. Control. Fusion **49**, 1913 (2007).